MICROBOONE-NOTE-1122-PUB

Measurement of Triple-Differential Inclusive Muon Neutrino Charged-Current Cross Sections on Argon with the MicroBooNE Detector

(The MicroBooNE Collaboration)*

(Dated: October 25, 2022)

We report the first measurement of the differential cross section $d^2\sigma(E_\nu)/dcos(\theta_\mu)dP_\mu$ for inclusive muon neutrino charged-current scattering on argon. This measurement utilizes data from 6.5×10^{20} protons on target of exposure collected using the MicroBooNE liquid argon time projection chamber located on-axis in the Fermilab Booster Neutrino Beam with a mean neutrino energy of approximately 0.8 GeV. In this note, the mapping from reconstructed kinematics to truth quantities, particularly from reconstructed to true neutrino energy, is validated by comparing the distribution of reconstructed hadronic energy in data to that of the model prediction in different muon scattering angle bins after conditional constraint from the muon momentum distribution in data. The success of this validation gives confidence that the missing energy in the MicroBooNE detector is well-modeled within its uncertainties in simulation, enabling the unfolding to an energy-dependent triple-differential measurement over muon momentum, muon scattering angle, and neutrino energy. The unfolded measurement covers an extensive phase space, providing a wealth of information useful for future LArTPC experiments measuring neutrino oscillations. Comparisons with model predictions show the best agreement with Neut 5.4.0.1 at low energy, and with NuWro 19.02.01 at higher energies, particularly at forward muon scattering angles.

* microboone_info@fnal.gov

Precision modeling of neutrino-nucleus interactions is necessary to achieve the goals of future accelerator neutrino oscillation experiments. In particular, the search for leptonic charge-parity (CP) violation may be limited by cross-section model uncertainties [1], as the measurement of oscillation parameters relies on accurate modeling of neutrino interactions [2, 3]. In the energy range of 0.1-5 GeV, the dominant modes of neutrino interactions can be difficult to model because of various nuclear effects. Typical examples include nuclear ground state modeling, nucleon-nucleon correlations, and final state interactions [4]. Efforts to simulate these interactions accurately would benefit from dedicated measurements that probe the relevant phase space. Since charged current (CC) neutrino interactions are predominant in measuring neutrino oscillations, it is important to validate neutrino interactions over a combined leptonic and hadronic kinematics phase space. For inclusive ν_μ CC scattering, there are three degrees of freedom determining the complete interaction kinematics: the scattering muon momentum (P_μ) and angle (θ_μ) that are directly measured, and the neutrino energy (E_ν) that is deduced with the measurement of the hadronic energy. The accurate reconstruction of the neutrino energy is of particular importance to flagship neutrino oscillation measurements [5, 6], which motivates this work.

There have been continuous advancements in the field of inclusive and exclusive neutrino-nucleus scattering (see Ref. [7–10] among others for recent progress). The measurement most relevant to this note is the triple-differential cross section [11] measured on carbon at MINERνA where the independent variables are the muon kinematics and the total observed proton energy. On an argon target, single and double differential ν_μ CC inclusive cross sections [12–15] have been reported. The measurement presented here expands upon the work measuring energy-dependent cross sections in Ref [15], which uses a measurement space of true neutrino energy. Specifically, we report the first measurement of a nominal-flux averaged inclusive ν_μ CC triple differential cross section on argon, measured over E_ν, P_μ, and $cos(\theta_\mu)$. Neutrino events are selected using the ν_μ selection described in [16] with $E_\nu \in [0.2, 4.0]$ GeV and $P_\mu \in [0, 2.5]$ GeV/c, giving an overall selection efficiency of 68% and purity of 92%. The estimation of the neutrino energy uses measurements of the visible hadronic energy (E^{rec}_{had}) and P_μ. Thanks to high statistics in this sample and comprehensive coverage of the 3D phase space, we extend the validation procedure first presented in [15] from single to multiple dimensions. The procedure works by comparing the reconstructed distribution in data with the model prediction through the use of χ^2 goodness-of-fit test statistics to demonstrate that the model uncertainties cover the difference between data and prediction.

The MicroBooNE detector is a 2.56 m (x) × 2.32 m (y) × 10.36 m (z) Liquid Argon Time Projection Chamber (LArTPC) filled with 85 tonnes of LAr that is capable of ∼mm-level position resolution as well as calorimetry with ∼MeV-level detection threshold. Ionization electrons drift in a 273 V/cm electric field towards an anode consisting of 3 detection planes of wires at 60° angles to each other with a wire pitch of 3 mm. 32 PMTs are used to detect the scintillation light from the interaction to provide a prompt timing signal. The detector is situated 470 m downstream of the Booster Neutrino Beam (BNB) at Fermilab, which accelerates protons up to 8 GeV in a synchrotron before colliding with a beryllium target. A magnetic horn focuses the produced π^+ and K^+ that create neutrinos with a peak E_ν of 0.8 GeV, with 93.6% estimated to be ν_μ.

The event selection used in this analysis is the same as used in one of the electron Low Energy Excess searches [16], and was performed on a data set collected from 2015-2018 using an exposure of 6.5×10^{20} protons on target (POT), an order of magnitude larger than the previous work [15]. The Wire-Cell reconstruction chain leverages the detector information through the use of tomography [17], many-to-many matching of TPC-charge clusters to PMT-light flashes, and trajectory fitting for particle identification and cosmic-ray removal [18]. Higher-level algorithms perform pattern recognition, neutrino vertex identification, topology classification, and particle identification to produce a particle flow within an event [19]. A boosted decision tree based library XGBoost [20] is then used to further reduce backgrounds to achieve the ν_μ CC selection. The selection is described in more detail in [16].

Energy reconstruction is crucial for the extraction of energy-dependent cross sections [15] as well as for the search for new physics beyond the Standard Model [16]. In general, energy reconstruction can be separated into the reconstruction of electromagnetic (EM) showers and of particle tracks. The estimation of EM shower energy is derived from the total associated charge with a scaling factor [21] of 2.5, which includes the overall mean recombination effect as well as contributions for clustering efficiency and detection threshold, and is validated through the reconstructed invariant mass of the neutral pion [22]. By default, particle tracks have their energy estimated from the propagation length using the Bethe-Bloch equations as tabulated in the NIST PSTAR database [23]. This method is substituted with a recombination-based approach in a few cases, including short tracks (< 4 cm), tracks exiting the detector, tracks with a "wiggled" topology [19], and muon tracks with identified δ rays. The recombination-based approach integrates the energy loss per unit length dE/dx along the particle track after converting from the measured dQ/dx [18] using a recombination model [24]. For the reconstruction of E_ν, the particle masses are taken into account as well as an average binding energy of 8.6 MeV per proton [25]. Energy resolutions are estimated from Monte Carlo (MC) simulation [26]. For ν_μ CC events that are fully contained (FC) within the detector, there is an estimated ∼10% resolution for muon energy, ∼30-50% for energy transfer resulting from imperfect reconstruction and missing hadronic energy $E^{missing}_{had}$, and ∼20% for E_ν. The angular resolution reaches 5^o in θ_μ at forward angles, but is less accurate at

backwards angles.

The neutrino flux prediction is derived from the MiniBooNE flux simulation [27] updated to the MicroBooNE detector location. It includes the production of p, n, $\pi^{\pm}$, $K^{\pm}$, and K^0_L from p-Be interactions, as well as their propagation using Geant4. Hadronic and EM re-interactions are modeled along with the effects of the magnetic field on particle trajectories. Neutrino production through meson decay is simulated including the effect of polarization of the mesons. Flux prediction uncertainties total to 5-15% over the flux range. Neutrino-argon (ν-Ar) interactions are modeled using GENIE version 3.0.6 G18_10a_02_11a tuned to T2K data [28], given the similar energy range. The modeling of hadronic interactions are conservatively estimated, with proton-to-neutron and proton knockout having 50% and 20% uncertainties respectively [29, 30], leading to an overall ∼20% ν-Ar interaction uncertainty. The modeling of uncertainties on flux, cross section, and secondary interactions of protons and charged pions outside the target nucleus (simulated with Geant4) are computed using a multisim technique [31] to calculate a covariance matrix. Additionally, there are uncertainties included for the model MC sample statistics that are estimated using the Poisson likelihood method [32], the modeling of "dirt" events originating outside the cryostat [33], the POT (2%) based on measurements of the originating proton flux [27], and the number of target nuclei (∼1%).

The detector response uncertainty considers the same effects as in the previous work [15, 34], taking into account the impact of variations in TPC waveform, light yield and propagation, the space charge effect [35, 36], and ionization recombination [24]. The overall detector response is estimated using the MicroBooNE model, where the simulated neutrino interactions are paired with measurements of cosmic events in data. This produces a sample with a high level of fidelity, but limits the quantity of simulation by the amount of background events available. To compensate for the limited MC statistics, the uncertainty in detector response is estimated using a unisim technique [37] to vary model parameters one at a time together with re-sampling of events through a bootstrapping procedure, discussed in Ref. [16]. For each effect listed above, a 1σ deviation in the parameter value is chosen based on observed variation within the data, and a fixed set of MC events is simulated both with the parameter central value (CV) and with the 1σ variation offset. These MC events are re-sampled to estimate the difference between CV and 1σ variation, called a difference vector, for each iteration. The mean of the difference vectors across all re-sampled iterations, $\vec{V}_D^{nominal}$, represents an estimator of 1σ uncertainty caused by the detector response, with corresponding covariance matrix M_R. Instances of $\vec{V}_D$ are generated by re-sampling from a normal distribution based on $\vec{V}_D^{nominal}$ and its uncertainty M_R for each detector effect to construct the overall detector response covariance matrix M_D.

Because of the large number of bins involved in a triple-differential analysis, the number of events per bin is small, causing the statistical fluctuations in $\vec{V}_D^{nominal}$ and therefore M_R and ultimately M_D to be very large. To address this, a Gaussian Processes Regression [38–40] (GPR) smoothing algorithm is applied to the distribution in $\vec{V}_D^{nominal}$, smoothing the statistical fluctuations introduced by the bootstrapping procedure. GPR uses a Bayesian approach to model the data with a joint Gaussian distribution and an uninformed prior. A smoothed posterior is computed from the simulated values of $\vec{V}_D^{nominal}$ as well as a kernel matrix Σ_K that asserts our intuition of smoothness between nearby bins through a radial basis kernel function $K(x_1, x_2) = e^{-|(\vec{x}_1 - \vec{x}_2)\cdot\vec{s}|^2/2}$. Based on reconstruction resolutions, length scales L_i were chosen to be 0.1 in $cos(\theta_\mu)$ and 20% for each of E_ν and P_μ to calculate $s_i = 1/L_i$. The central value and covariance of the posterior prediction are used in place of the original $\vec{V}_D^{nominal}$ and M_R. Because of GPR smoothing, statistical fluctuations are controlled and become less impactful in M_D, reducing the overall detector response covariance from ∼100% to ∼50%. The validity of this reduction is tested through the data/MC goodness-of-fit (GoF) tests.

Since the MicroBooNE model is used to estimate the selection efficiency and unfold the reconstructed variables such as E_ν^{rec} to truth quantities, it is important to validate its accuracy. If the model (including uncertainties) is unable to describe the distribution in data, it may introduce significant bias beyond the uncertainties into the extracted cross sections. Therefore, a comprehensive set of data/MC comparisons using the reconstructed kinematic variables P_μ, $cos(\theta_\mu)$, and the energy transferred to the hadronic system, E_{had}^{rec}, are investigated demonstrating the validity of the model. This procedure extends the work in Ref. [15] to multi-dimensional distributions to probe the 3D phase space being unfolded.

Because of the existence of missing energy (e.g. undetected neutrons and particles below the detection threshold), the mapping from reconstructed to truth E_ν needs special attention. This mapping can be tested through the combination of a GoF test over the muon kinematics with a GoF test over E_{had}^{rec}. The first test, shown in Fig. 4 in Appendix C, over the 2D $\{P_\mu, cos(\theta_\mu)\}$ distribution, gives a χ^2/ndf of 99/144, demonstrating that the model is able to describe the muon kinematics distribution seen in data well within the model uncertainties. The second test, shown in Fig. 1, is performed over the 2D $\{E_{had}^{rec}, cos(\theta_\mu)\}$ distribution and is constrained by the muon kinematics measurement using the conditional constraint formalism [41]. It similarly demonstrates a χ^2/ndf of 123/144 after applying the constraint, indicating that the model describes the relationship between $\{P_\mu, cos(\theta_\mu)\}$ and E_{had}^{rec} in data within its uncertainty. The constraint highly suppresses the common uncertainties between these distributions, such as those in the flux prediction, causing the posterior prediction to have much lower uncertainties and leading to a more stringent

examination of the model. The model validation tests showing an accurate description of muon kinematics, combined with the accurate modeling of E^{rec}_{had} in relation to $\{P_\mu, cos(\theta_\mu)\}$, validates the modeling of the missing hadronic energy to describe the data within its uncertainty, and ensures that the unfolding does not introduce bias beyond quoted uncertainties.

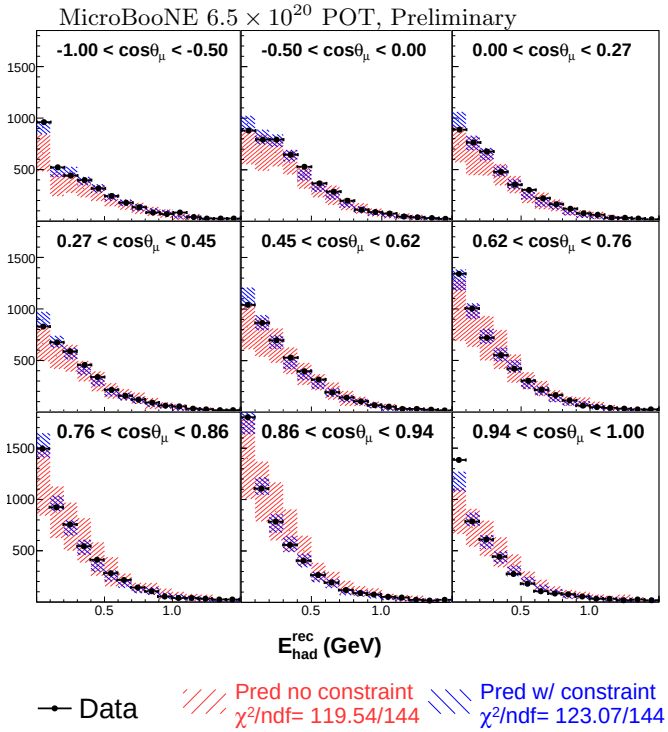

FIG. 1. Distribution of data and prediction over the 2D reco-space binning of $\{E^{rec}_{had}, \cos(\theta_\mu)\}$ for fully contained events. The MicroBooNE model prediction, including before (red) and after (blue) applying the measurement of the data distribution over $\{P_\mu, \cos(\theta_\mu)\}$ as a constraint, are quantitatively compared with data.

The triple-differential cross section is extracted using Wiener-SVD unfolding [42] with the equation:

$$M_i - B_i = \sum_j R_{ij} \cdot S_j = \sum_j \widetilde{\Delta}_{ij} \cdot \widetilde{F}_j \cdot S_j. \tag{1}$$

where M_i and B_i are the number of measured events and expected background events respectively in reconstructed bin i, and S_j is the signal vector in truth bin j. The response matrix R_{ij} can be separated into $\widetilde{\Delta}_{ij}$, the fraction of events that are generated in bin j and reconstructed and selected in bin i, computed from the distribution of MC events, and a constant $\widetilde{F}_j$ that is calculated from the POT, number of argon nuclei, integrated ν_μ flux in bin j, and bin width. The unfolding is performed by minimizing a test statistic:

$$\chi^2 = (M - B - R \cdot S)^T \cdot V^{-1} \cdot (M - B - R \cdot S) + T_{reg} \tag{2}$$

where V is the total covariance matrix of the measured number of events in the reconstructed binning. T_{reg} is a regularization term constructed using the Wiener filter [42] and the third derivative of the unfolded distribution w.r.t. each E_ν, $cos(\theta_\mu)$, and P_μ, which are further combined in quadrature. The covariance matrix includes statistical uncertainties, computed using the combined Neyman-Pearson method [43], as well as systematic uncertainties for signal and background events. The bias introduced in unfolding and regularization is captured in an additional smearing matrix A_C that is applied to every theoretical prediction.

The unfolded cross section consists of 138 bins spanning 4 E_ν slices, 9 $cos(\theta_\mu)$ slices, and 3-6 P_μ bins within each $\{E_\nu, cos(\theta_\mu)\}$ slice based on the statistics available. The binning was chosen by taking as a starting point the $cos(\theta_\mu)$ and P_μ binning from the previous double-differential cross section analysis [14] and the E_ν binning from the previous energy-dependent differential cross section analysis [15], both of which are chosen in accordance with the MicroBooNE detector resolution. To maintain adequate statistics in each bin, we first merge some E_ν bins, and then determine the allowed number of P_μ bins within a given $\{E_\nu, cos(\theta_\mu)\}$ slice. The full differential cross section is shown in Fig. 2,

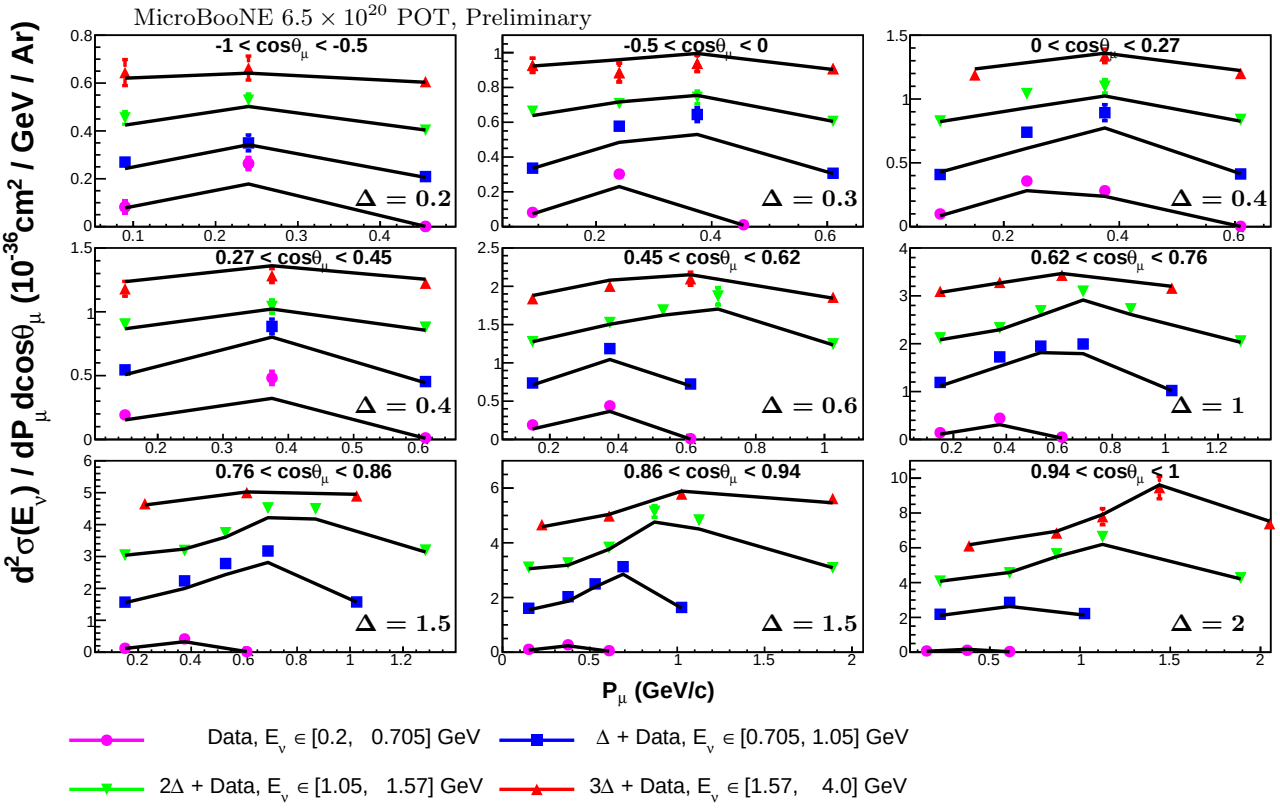

FIG. 2. Unfolded differential cross section measurement and NuWro prediction, chosen for having the lowest χ^2, are shown within each angle slice and with each E_ν measurement overlaid and offset to visually separate them. The magnitude of the offset Δ, given in the same units of $10^{-36}\text{cm}^2/\text{GeV}/\text{Ar}$, is listed in the bottom right of each plot.

TABLE I. Comparisons between various models and the unfolded triple-differential measurement.

Model Name	χ^2/ndf
GENIE v2.12.10	740.8/138
GENIE 3.0.6 G18_10a_02_11a (MicroBooNE tune)	313.9/138
GENIE 3.0.6 G18_10a_02_11a (untuned)	309.7/138
GiBUU 2021	265.6/138
NEUT 5.4.0.1	233.1/138
NuWro 19.02.01	200.9/138

where the 9 windows correspond to increasingly forward-angle slices, and within each window the P_μ distribution is plotted for each of the four E_ν slices, offset by an arbitrary scaling (Δ) for visual clarity. The data is plotted against the NuWro 19.02.01 prediction, which has the best agreement with the data, as measured by the χ^2 listed in Table I.

Table I gives comparisons with model predictions for GENIE v2.12.10, GENIE 3.0.6 G18_10a_02_11a [29, 44], NuWro 19.02.01 [45], NEUT 5.4.0.1 [46], and GiBUU 2021 [47]. A comparison of the underlying physics models in these event generators can be found in Ref. [48]. The unfolded triple-differential measurement is found to be in tension with all model CV predictions. NEUT and NuWro show the best agreement, followed by GiBUU, broadly similar to the hierarchy of agreement found previously in the single-differential analysis[15]. Owing to the improved level of detail available across the 3D phase space, the power of these results in differentiating models is significantly improved with respect to the previous single differential analysis [15]. To illustrate this point, the differential cross sections over $cos(\theta_\mu)$ and E_ν, constructed by integrating over P_μ and normalizing by the average neutrino energy $\langle E_\nu \rangle$, are plotted in Fig. 3. A primary advantage comes from the subdivision by neutrino energy, resulting in a better separation between the quasi-elastic and pion production processes. The quasi-elastic fraction decreases from $\sim$ 75% in the lowest energy bin to $\sim$ 55% in the highest energy bin as predicted by NuWro (see Appendix C Fig. 10 for details). While NEUT performs well at low neutrino energy, the region most similar to the T2K dataset that it was tuned

on, GENIE v3.0.6 and NuWro have the best by-eye agreement at higher energies and particularly at forward angles. This is a region with larger delta-resonant contributions where notable differences in pion production modelling exist, especially at low Q^2 and forward lepton angles [49].

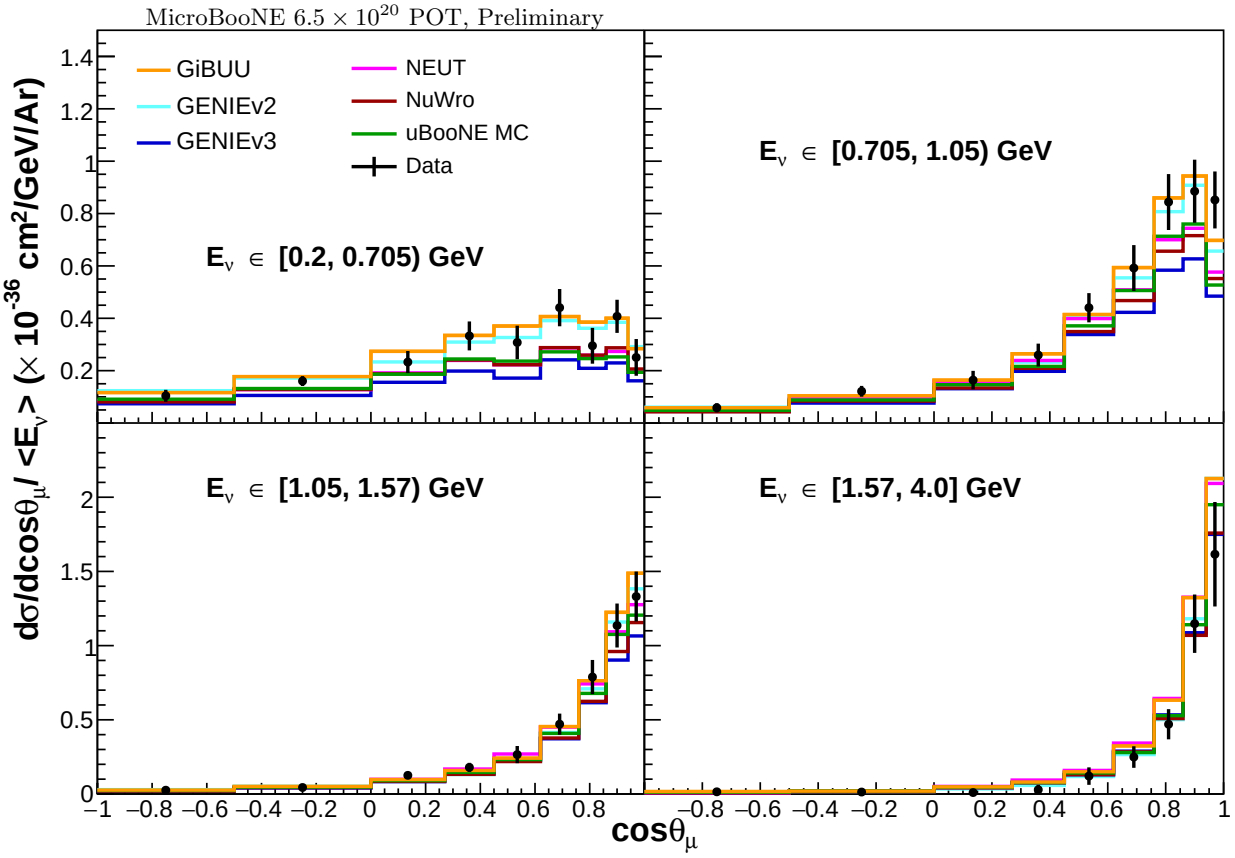

FIG. 3. Unfolded differential cross section over $cos(\theta_\mu)$ after integrating over P_μ and normalizing by the average $\langle E_\nu \rangle$ in each E_ν bin.

In summary, we report the nominal-flux averaged differential inclusive ν_μ CC cross section $d^2\sigma(E_\nu)/d\cos(\theta\mu)dP_\mu$, baswaed on an exposure of 6.5×10^{20} POT of data from the Booster Neutrino Beam at Fermilab. This work advances the field of LArTPC experiments by providing the first measurement over a complete 3D kinematic phase space for the inclusive ν_μ CC channel. This allows for a better understanding of the models and their contributions across the available phase space. This measurement can be further expanded on in future analyses through exclusive channel measurements, as well as through increased statistics from the both the roughly doubling of total MicroBooNE data available and the combination of BNB and NuMI data taken at MicroBooNE. Looking further ahead, the SBN program will provide an order of magnitude more data, allowing for even more precise cross section measurements.

ACKNOWLEDGMENTS

This document was prepared by the MicroBooNE collaboration using the resources of the Fermi National Accelerator Laboratory (Fermilab), a U.S. Department of Energy, Office of Science, HEP User Facility. Fermilab is managed by Fermi Research Alliance, LLC (FRA), acting under Contract No. DE-AC02-07CH11359. MicroBooNE is supported by the following: the U.S. Department of Energy, Office of Science, Offices of High Energy Physics and Nuclear Physics; the U.S. National Science Foundation; the Swiss National Science Foundation; the Science and Technology Facilities Council (STFC), part of the United Kingdom Research and Innovation; the Royal Society (United Kingdom); and the UK Research and Innovation (UKRI) Future Leaders Fellowship. Additional support for the laser calibration system and cosmic ray tagger was provided by the Albert Einstein Center for Fundamental Physics, Bern, Switzerland. We also acknowledge the contributions of technical and scientific staff to the design, construction, and operation of the MicroBooNE detector as well as the contributions of past collaborators to the development of MicroBooNE analyses, without whom this work would not have been possible.

Appendix A: Goodness of Fit Plots

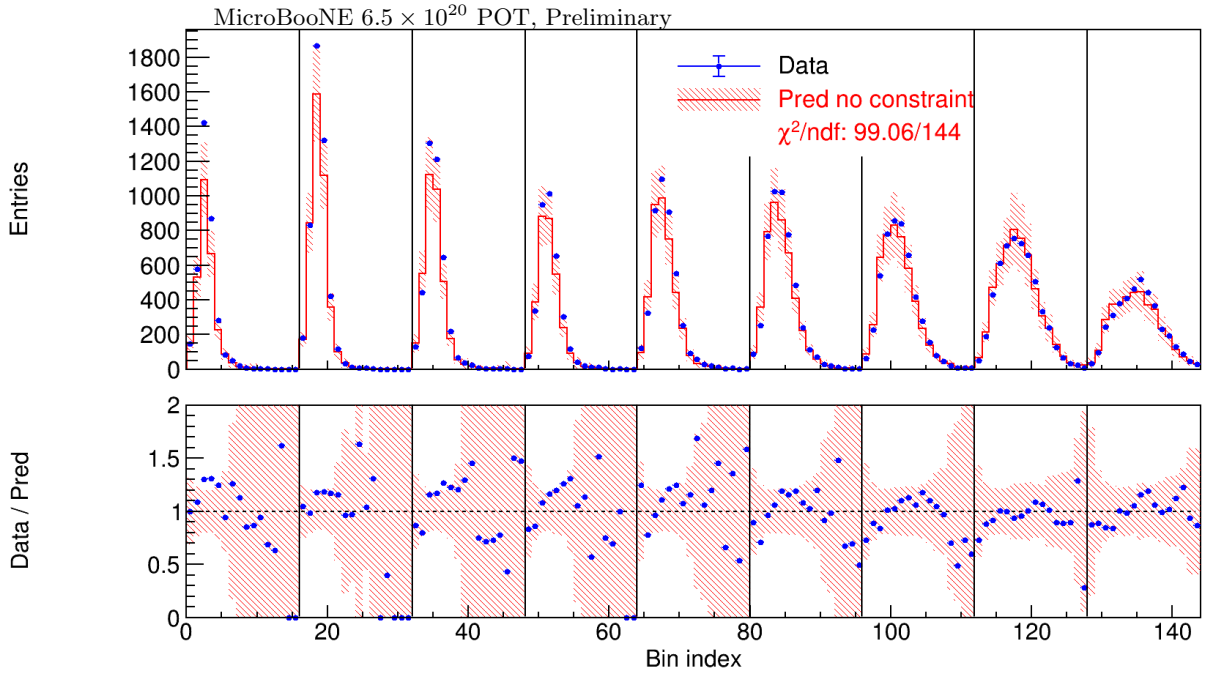

(a)

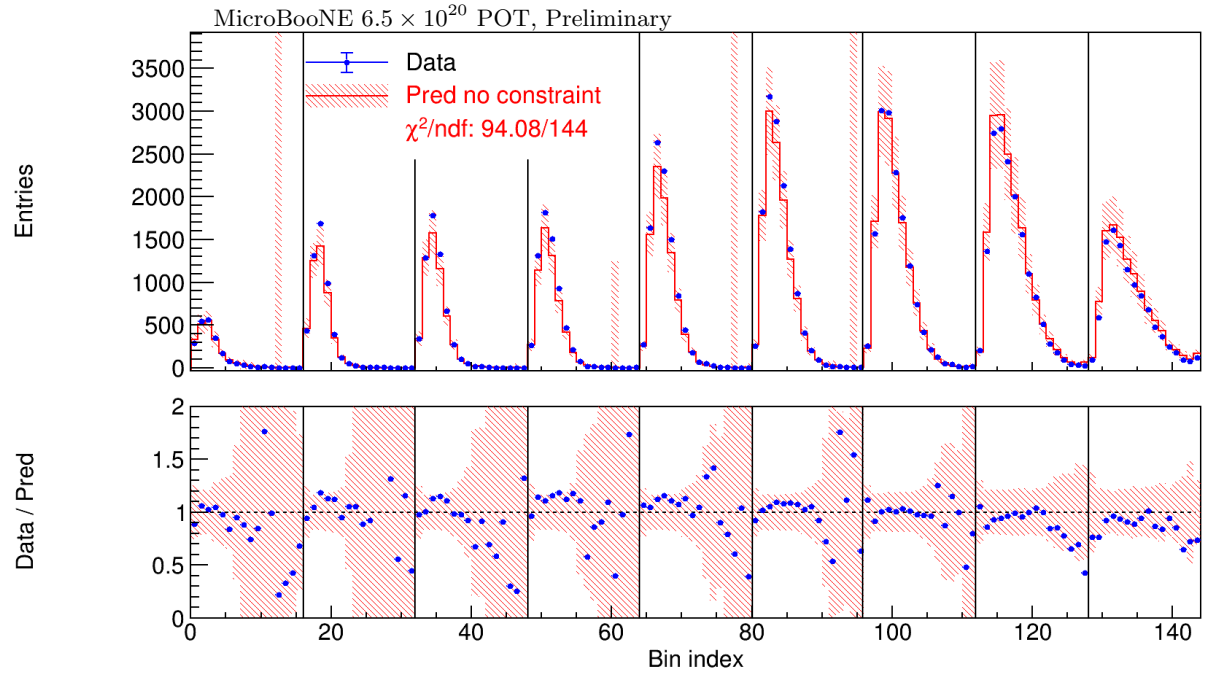

(b)

FIG. 4. Distribution of data and prediction over the 2D reco-space binning of $\{P_\mu, \cos(\theta_\mu)\}$ for fully contained (top) and partially contained (bottom) events. The MicroBooNE model prediction is quantitatively compared with data.

To ensure that the unfolded cross sections have sufficient uncertainties listed, it is important to demonstrate that the MicroBooNE model prediction and uncertainties cover the distribution seen in data. Figs. 4 and 5 demonstrate model validation over different kinematic distributions. In each case, a $\chi^2/\text{ndf} < 1$ indicates sufficient coverage of model

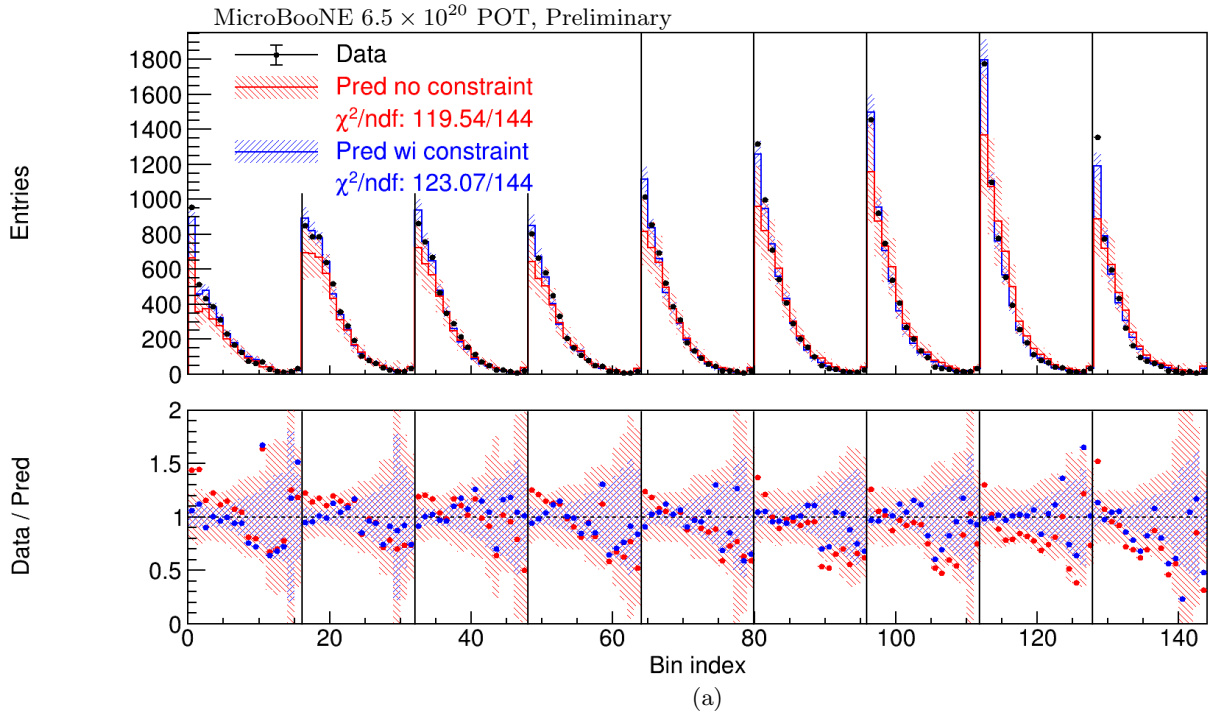

(a)

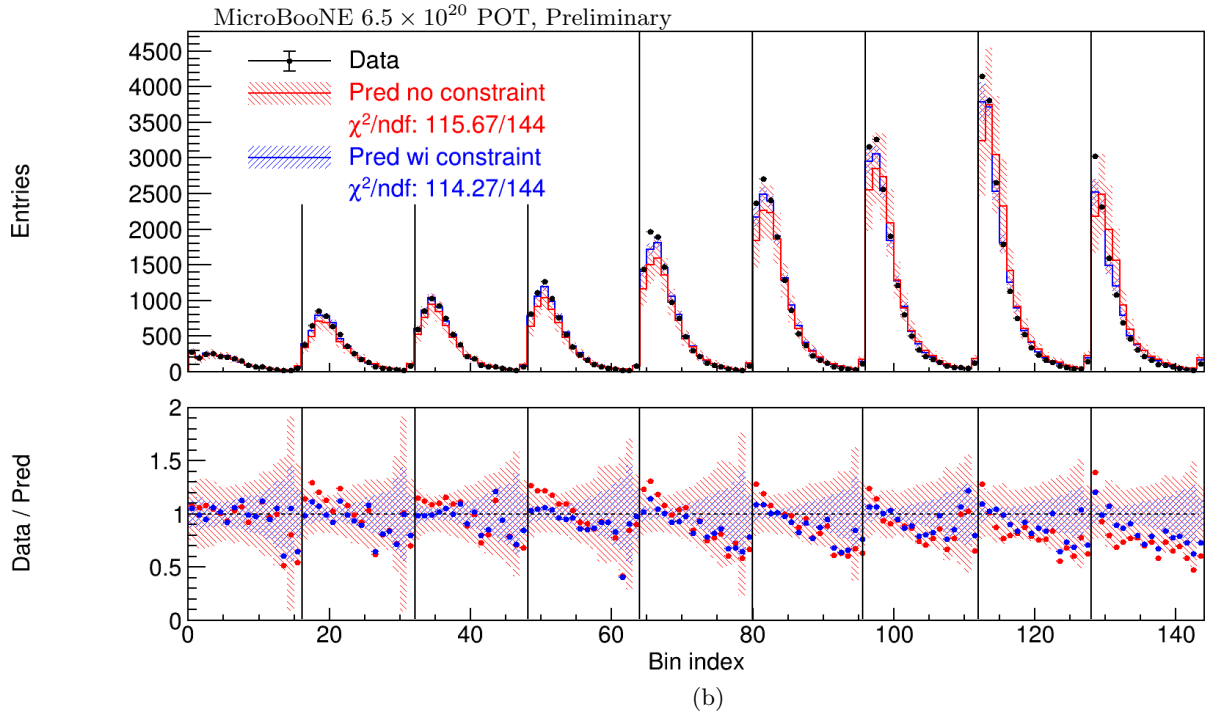

(b)

FIG. 5. Distribution of data and prediction over the 2D reco-space binning of $\{E_{had}^{rec}, \cos(\theta_\mu)\}$ for fully contained (top) and partially contained (bottom) events. The MicroBooNE model prediction, including before (red) and after (blue) applying the measurement of the data distribution over $\{P_\mu, \cos(\theta_\mu)\}$ as a constraint, are quantitatively compared with data.

uncertainties. The event selection is divided into fully- and partially-contained events, based on whether neutrino interaction activity resides fully within the detector fiducial volume. The 9 angle slices are plotted side-by-side, separated by vertical black bars, and arranged from backward to forward facing. The angle slice edges are given by $cos(\theta_\mu) \in \{-1, -0.5, 0, 0.27, 0.45, 0.62, 0.76, 0.86, 0.94, 1\}$. Within each angle slice are 15 P_μ bins 100 MeV/c wide plus an overflow bin up to 2500 MeV.

Appendix B: Uncertainties Breakdown

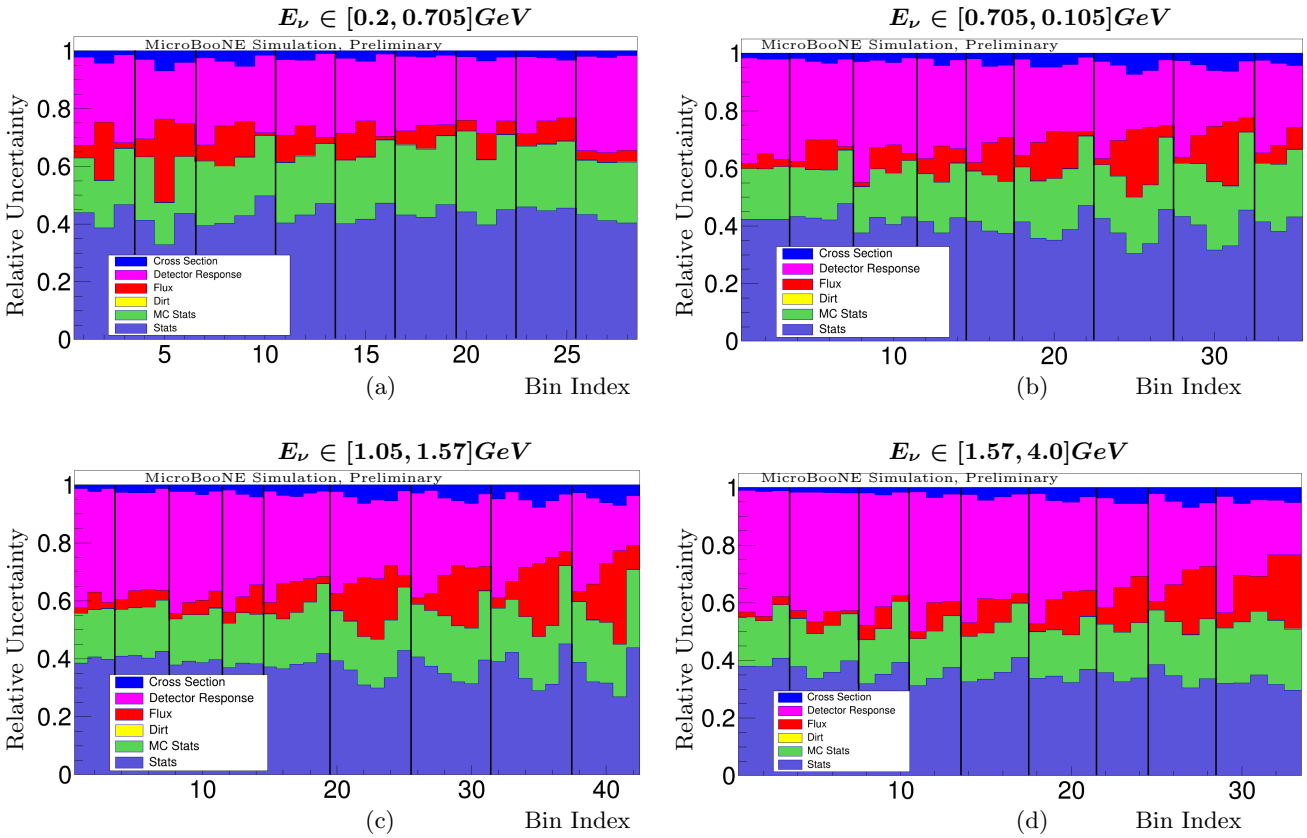

FIG. 6. Breakdown of unfolded uncertainties by type over the unfolded 3D binning. Each subplot corresponds to the 2D bin index over $\{P_\mu, cos(\theta_\mu)\}$ within each E_ν slice. Each subplot has a different number of bins corresponding to the variable number of P_μ bins in each angle slice, which are separated by vertical black bars, and arranged from backward to forward facing. The angle slice edges are given by $cos(\theta_\mu) \in \{-1, -0.5, 0, 0.27, 0.45, 0.62, 0.76, 0.86, 0.94, 1\}$.

These plots show the breakdown of uncertainties across the 138 unfolded measurement bins. Each subplot corresponds to the $\{P_\mu, cos(\theta_\mu)\}$ bins within a different E_ν slice.

Appendix C: Unfolded Multi-Differential Cross Section Results

Fig. 7, Fig. 8, and Fig. 9 are re-visualizations of the data presented in Fig. 2, and include model predictions for all generators, the MicroBooNE model, and the NuWro model respectively. They show the data (with uncertainties) against various model predictions over a spacial representation of the 3D phase space. Fig 10 shows the multi-differential cross section measurement against the NuWro model prediction, similar to Fig. 2. The NuWro prediction is broken down into each interaction channel to show the size of each channel's contribution to each measurement bin. This measurement is then integrated over the P_μ dimension to produce a 2D measurement shown in Fig 11 that parallels Fig. 3. Again, the NuWro prediction is broken down into each interaction channel to show the size of each channel contributions to each measurement bin.

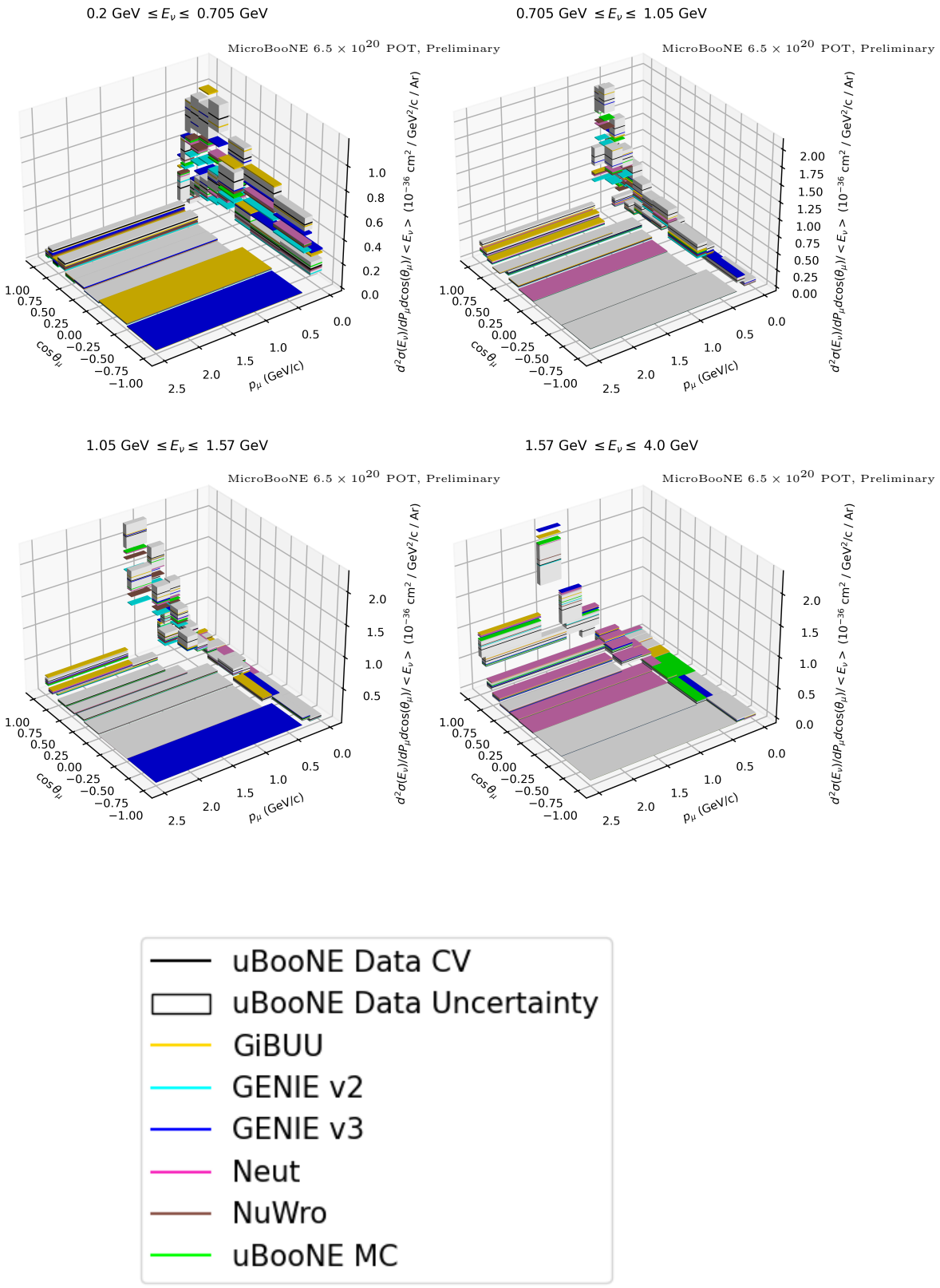

FIG. 7. Unfolded cross section measurement shown over $\{P_\mu, cos(\theta_\mu)\}$ for each E_ν slice. Data with uncertainties is plotted against each model prediction.

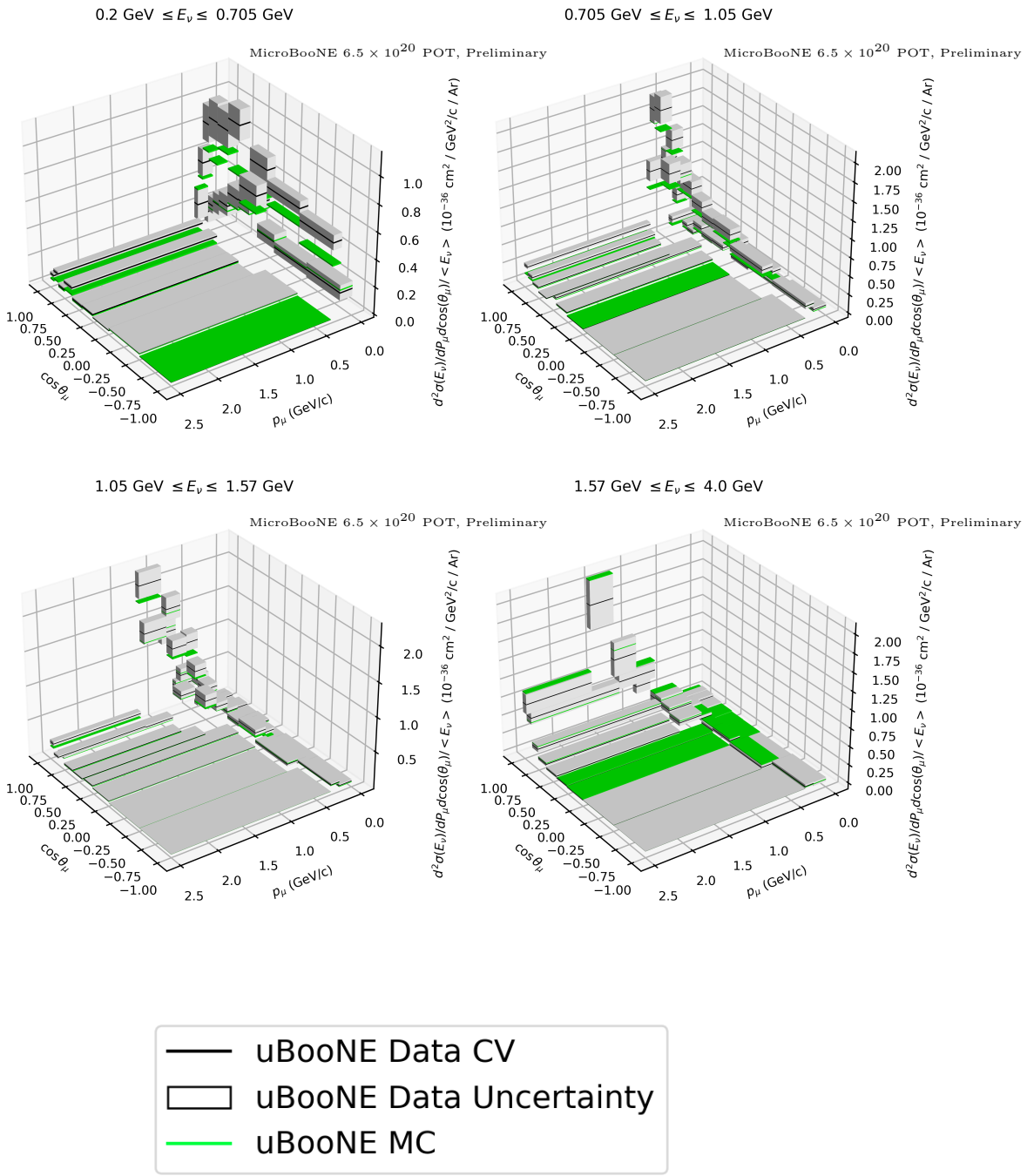

FIG. 8. Unfolded cross section measurement shown over $\{P_\mu, cos(\theta_\mu)\}$ for each E_ν slice. Data with uncertainties is plotted against the MicroBooNE model prediction.

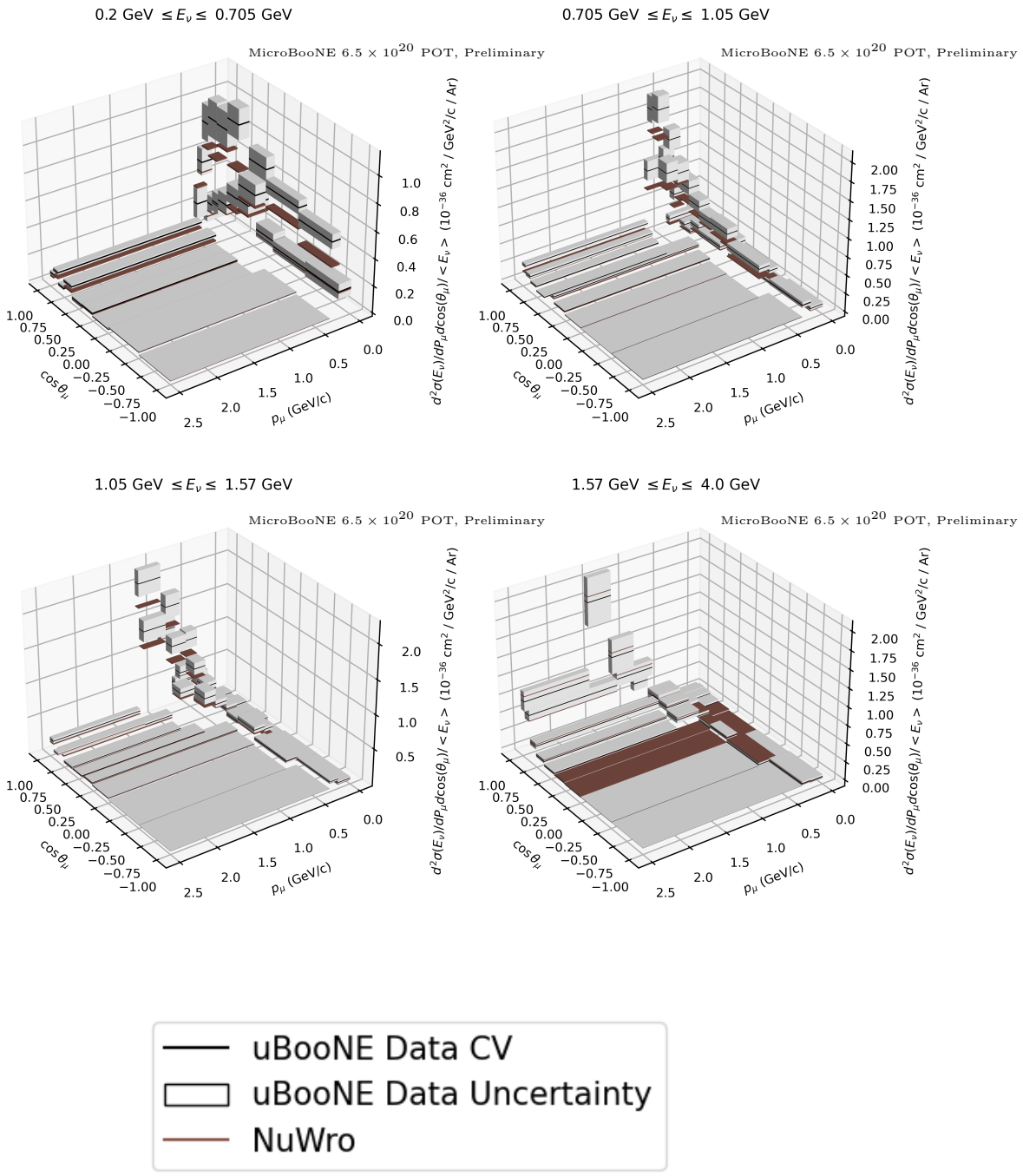

FIG. 9. Unfolded cross section measurement shown over $\{P_\mu, cos(\theta_\mu)\}$ for each E_ν slice. Data with uncertainties is plotted against the NuWro model prediction.

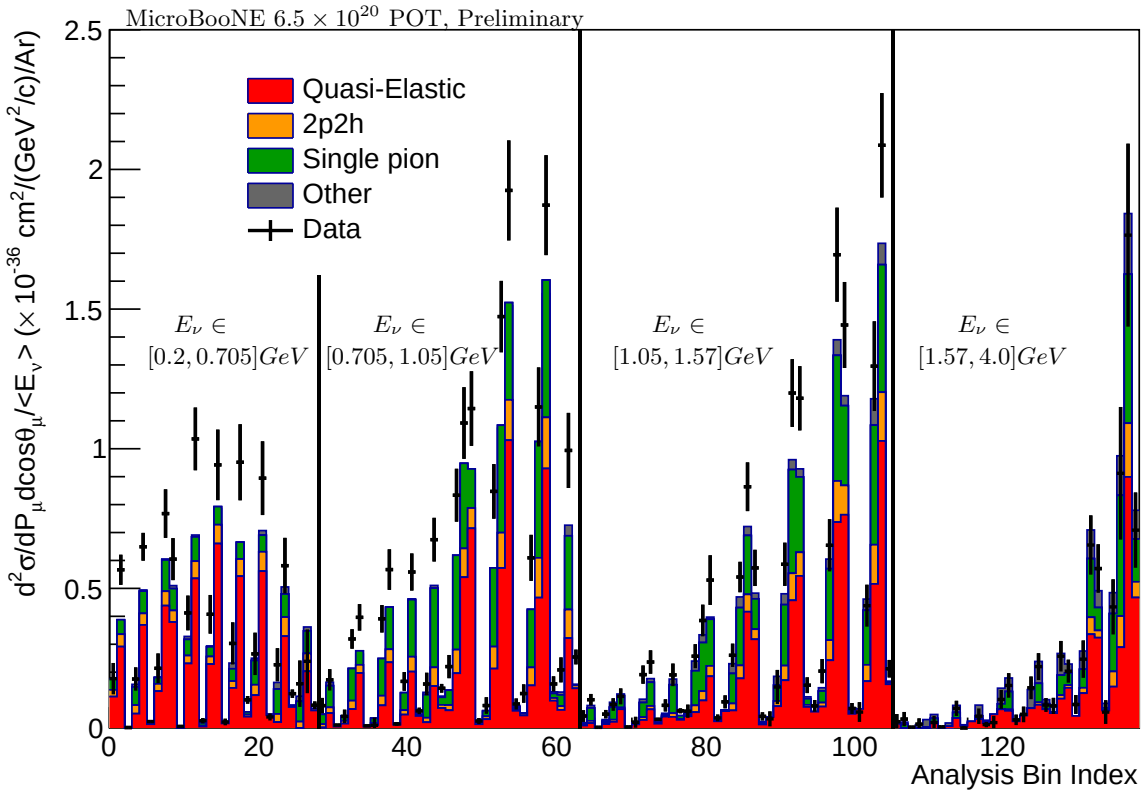

FIG. 10. Unfolded cross-section measurement shown over the full 138 bin space, plotted against the NuWro prediction with breakdown by interaction channel. The four E_ν slices are separated by vertical black bars. Within each E_ν slice the nine angle slices are plotted from backward to forward, with P_μ bins in each angle slice.

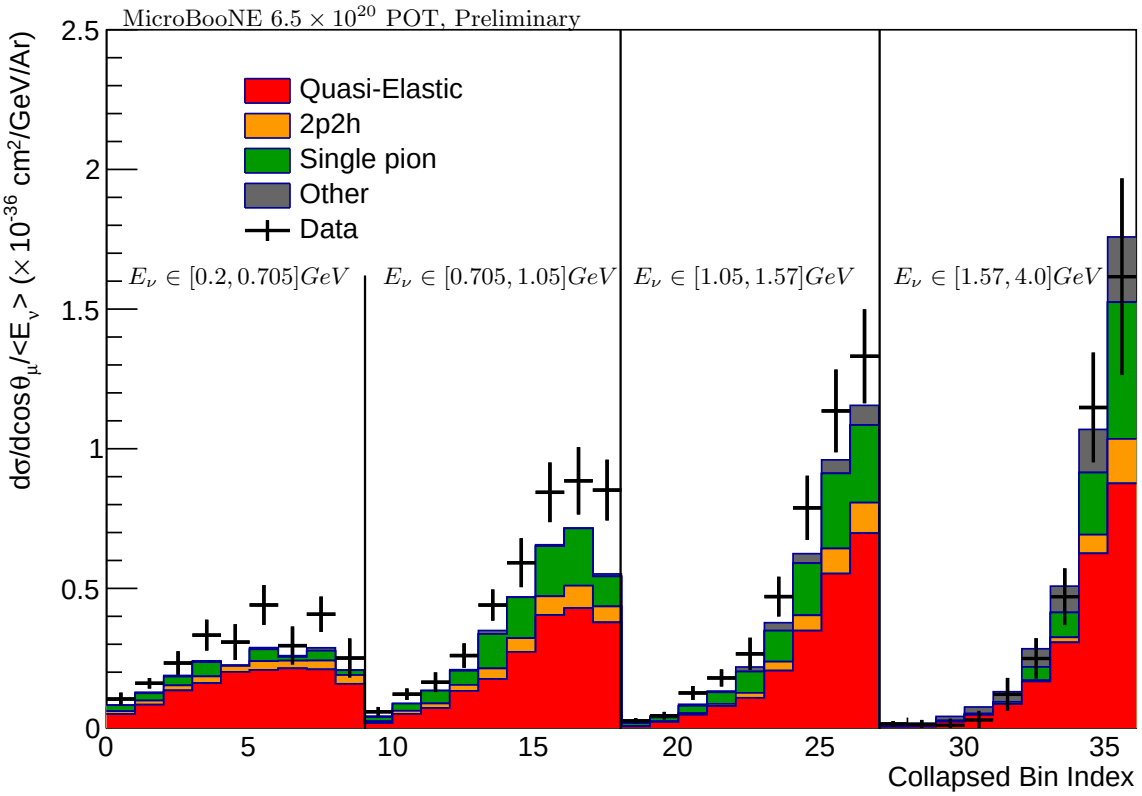

FIG. 11. Unfolded cross-section measurement shown over the 2D $\{E_\nu, cos(\theta_\mu)\}$ phase space, plotted against the NuWro prediction with breakdown by interaction channel. The four E_ν slices are separated by vertical black bars. Within each slice, the angle bin edges are given by $cos(\theta_\mu) \in \{-1, -0.5, 0, 0.27, 0.45, 0.62, 0.76, 0.86, 0.94, 1\}$.

[1] S. Nagu, J. Singh, J. Singh, and R. Singh, Impact of cross-sectional uncertainties on DUNE sensitivity due to nuclear effects, Nuclear Physics B **951**, 114888 (2020).

[2] P. F. de Salas, D. V. Forero, S. Gariazzo, P. Martínez-Miravé, O. Mena, C. A. Ternes, M. Tórtola, and J. W. F. Valle, 2020 global reassessment of the neutrino oscillation picture, JHEP **02**, 071, arXiv:2006.11237 [hep-ph].

[3] R. L. Workman and Others (Particle Data Group), Review of Particle Physics, PTEP **2022**, 083C01 (2022).

[4] J. A. Formaggio and G. P. Zeller, From eV to EeV: Neutrino cross sections across energy scales, Rev. Mod. Phys. **84**, 1307 (2012).

[5] B. Abi *et al.*, Volume i. introduction to DUNE, Journal of Instrumentation **15** (08), T08008.

[6] M. Antonello *et al.* (MicroBooNE, LAr1-ND, ICARUS-WA104), A Proposal for a Three Detector Short-Baseline Neutrino Oscillation Program in the Fermilab Booster Neutrino Beam (2015) arXiv:1503.01520 [physics.ins-det].

[7] D. Ruterbories *et al.* (MINERvA Collaboration), Measurement of inclusive charged-current ν_μ cross sections as a function of muon kinematics at $< E_\nu > \sim 6\ GeV$ on hydrocarbon, Phys. Rev. D **104**, 092007 (2021), arXiv:2106.16210 [hep-ex].

[8] A. Bercellie *et al.* (MINERvA Collaboration), Simultaneous measurement of muon neutrino ν_μ charged-current single π^+ production in CH, C, H_2O, Fe, and Pb targets in MINERvA, arXiv:2209.07852 [hep-ex] (2022).

[9] K. Abe *et al.* (T2K Collaboration), Simultaneous measurement of the muon neutrino charged-current cross section on oxygen and carbon without pions in the final state at T2K, Phys. Rev. D **101**, 112004 (2020), arXiv:2004.05434 [hep-ex].

[10] K. Abe *et al.* (T2K Collaboration), Measurements of $\overline{\nu}_\mu$ and $\overline{\nu}_\mu + \nu_\mu$ charged-current cross-sections without detected pions or protons on water and hydrocarbon at a mean anti-neutrino energy of 0.86 GeV, PTEP **2021**, 043C01 (2021), arXiv:2004.13989 [hep-ex].

[11] D. Ruterbories *et al.* (MINERvA Collaboration), Simultaneous Measurement of Proton and Lepton Kinematics in Quasielasticlike ν_μ-Hydrocarbon Interactions from 2 to 20 GeV, Phys. Rev. Lett. **129**, 021803 (2022), arXiv:2203.08022 [hep-ex].

[12] C. Anderson *et al.* (ArgoNeuT Collaboration), First measurements of inclusive muon neutrino charged current differential cross sections on argon, Phys. Rev. Lett. **108**, 161802 (2012).

[13] R. Acciarri *et al.* (MicroBooNE Collaboration), Measurements of inclusive muon neutrino and antineutrino charged current differential cross sections on argon in the NuMI antineutrino beam, Physical Review D **89**, 10.1103/physrevd.89.112003 (2014).

[14] P. Abratenko *et al.* (MicroBooNE Collaboration), First Measurement of Inclusive Muon Neutrino Charged Current Differential Cross Sections on Argon at Enu Approximately 0.8 GeV with the MicroBooNE Detector, Physical Review Letters **123**, 10.1103/physrevlett.123.131801 (2019).

[15] P. Abratenko *et al.* (MicroBooNE Collaboration), First measurement of energy-dependent inclusive muon neutrino charged-current cross sections on argon with the MicroBooNE detector, Physical Review Letters **128**, 10.1103/physrevlett.128.151801 (2022).

[16] P. Abratenko *et al.* (MicroBooNE Collaboration), Search for an anomalous excess of inclusive charged-current ν_e interactions in the MicroBooNE experiment using Wire-Cell reconstruction, `https://microboone.fnal.gov/electron_analysis_1ex_2021/` (2021).

[17] X. Qian, C. Zhang, B. Viren, and M. Diwan, Three-dimensional Imaging for Large LArTPCs, JINST **13** (05), P05032.

[18] P. Abratenko *et al.* (MicroBooNE Collaboration), Cosmic Ray Background Rejection with Wire-Cell LArTPC Event Reconstruction in the MicroBooNE Detector, Phys. Rev. Applied **15**, 064071 (2021), arXiv:2101.05076 [physics.ins-det].

[19] P. Abratenko *et al.* (MicroBooNE Collaboration), Wire-cell 3D pattern recognition techniques for neutrino event reconstruction in large LArTPCs: algorithm description and quantitative evaluation with MicroBooNE simulation, Journal of Instrumentation **17** (01), P01037.

[20] T. Chen and C. Guestrin, XGBoost: A Scalable Tree Boosting System (2016) arXiv:1603.02754 [cs.LG].

[21] P. Abratenko *et al.* (MicroBooNE Collaboration), Neutrino event selection in the MicroBooNE liquid argon time projection chamber using Wire-Cell 3D imaging, clustering, and charge-light matching, JINST **16** (06), P06043, arXiv:2011.01375 [physics.ins-det].

[22] C. Adams *et al.* (MicroBooNE Collaboration), Reconstruction and Measurement of $\mathcal{O}(100)$ MeV Energy Electromagnetic Activity from $\pi^0 \to \gamma\gamma$ Decays in the MicroBooNE LArTPC, JINST **15** (02), P02007.

[23] PSTAR at NIST: `https://physics.nist.gov/PhysRefData/Star/Text/PSTAR.html`.

[24] C. Adams *et al.* (MicroBooNE Collaboration), Calibration of the Charge and Energy Response of the MicroBooNE Liquid Argon Time Projection Chamber using Muons and Protons, JINST **15** (03), P03022.

[25] S. Sukhoruchkin and Z. Soroko, Atomic mass and nuclear binding energy for ar-40 (argon): Datasheet from landolt-börnstein - group i elementary particles, nuclei and atoms · volume 22a: "nuclei with z = 1 - 54" in springermaterials (https://doi.org/10.1007/978-3-540-69945-3_558), copyright 2009 Springer-Verlag Berlin Heidelberg.

[26] P. Abratenko *et al.* (MicroBooNE Collaboration), New Theory-driven GENIE Tune for MicroBooNE (2021) arXiv:2110.14028 [hep-ex].

[27] A. A. Aguilar-Arevalo *et al.* (MiniBooNE Collaboration), The Neutrino Flux prediction at MiniBooNE, Phys. Rev. D **79**, 072002 (2009), arXiv:0806.1449 [hep-ex].

[28] K. Abe *et al.* (T2K Collaboration), Measurement of double-differential muon neutrino charged-current interactions on C_8H_8 without pions in the final state using the T2K off-axis beam, Phys. Rev. D **93**, 112012 (2016), arXiv:1602.03652 [hep-ex].

[29] C. Andreopoulos *et al.*, The GENIE Neutrino Monte Carlo Generator, Nucl. Instrum. Meth. A **614**, 87 (2010), arXiv:0905.2517 [hep-ph].

[30] C. Andreopoulos, C. Barry, S. Dytman, H. Gallagher, T. Golan, R. Hatcher, G. Perdue, and J. Yarba (GENIE Collaboration), The GENIE Neutrino Monte Carlo Generator: Physics and User Manual (2015), arXiv:1510.05494 [hep-ph].

[31] B. P. Roe, Statistical errors in monte carlo estimates of systematic errors, Nuclear Instruments and Methods in Physics Research Section A: Accelerators, Spectrometers, Detectors and Associated Equipment **570**, 159 (2007).

[32] C. A. Argüelles, A. Schneider, and T. Yuan, A binned likelihood for stochastic models, JHEP **06**, 030, arXiv:1901.04645 [physics.data-an].

[33] P. Abratenko *et al.* (MicroBooNE Collaboration), Search for an anomalous excess of inclusive charged-current ν_e interactions in the MicroBooNE experiment using Wire-Cell reconstruction (2021) arXiv:2110.13978 [hep-ex].

[34] P. Abratenko *et al.*, Novel approach for evaluating detector-related uncertainties in a LArTPC using MicroBooNE data, Eur. Phys. J. C **82**, 454 (2022).

[35] P. Abratenko *et al.* (MicroBooNE Collaboration), Measurement of space charge effects in the MicroBooNE LArTPC using cosmic muons, JINST **15** (12), P12037, arXiv:2008.09765 [physics.ins-det].

[36] C. Adams *et al.* (MicroBooNE Collaboration), A Method to Determine the Electric Field of Liquid Argon Time Projection Chambers Using a UV Laser System and its Application in MicroBooNE, JINST **15** (07), P07010.

[37] B. P.Roe, Statistical errors in Monte Carlo estimates of systematic errors, Nuclear Instruments and Methods in Physics Research Section A **570**, 159 (2006).

[38] C. E. Rasmussen and C. K. I. Williams, *Gaussian Processes for Machine Learning (Adaptive Computation and Machine Learning)* (The MIT Press, 2005).

[39] M. Frate, K. Cranmer, S. Kalia, A. Vandenberg-Rodes, and D. Whiteson, Modeling smooth backgrounds and generic localized signals with gaussian processes (2017).

[40] L. Li, N. Nayak, J. Bian, and P. Baldi, Efficient neutrino oscillation parameter inference using Gaussian processes, Phys. Rev. D **101**, 012001 (2020).

[41] M. L. Eaton, Multivariate statistics: a vector space approach, John Wiley and Sons , 116 (1983).

[42] W. Tang, X. Li, X. Qian, H. Wei, and C. Zhang, Data Unfolding with Wiener-SVD Method, JINST **12** (10), P10002, arXiv:1705.03568 [physics.data-an].

[43] X. Ji, W. Gu, X. Qian, H. Wei, and C. Zhang, Combined Neyman–Pearson chi-square: An improved approximation to the Poisson-likelihood chi-square, Nucl. Instrum. Meth. A **961**, 163677 (2020), arXiv:1903.07185 [physics.data-an].

[44] L. Alvarez-Ruso *et al.* (GENIE Collaboration), Recent highlights from GENIE v3 (2021) arXiv:2106.09381 [hep-ph].

[45] T. Golan, J. T. Sobczyk, and J. Zmuda, NuWro: the Wroclaw Monte Carlo Generator of Neutrino Interactions, Nucl. Phys. B Proc. Suppl. **229-232**, 499 (2012).

[46] Y. Hayato, A neutrino interaction simulation program library NEUT, Acta Phys. Polon. B **40**, 2477 (2009).

[47] O. Buss, T. Gaitanos, K. Gallmeister, H. van Hees, M. Kaskulov, O. Lalakulich, A. B. Larionov, T. Leitner, J. Weil, and U. Mosel, Transport-theoretical Description of Nuclear Reactions, Phys. Rept. **512**, 1 (2012), arXiv:1106.1344 [hep-ph].

[48] M. B. Avanzini *et al.*, Comparisons and challenges of modern neutrino-scattering experiments, Phys. Rev. D **105**, 092004 (2022), arXiv:2112.09194 [hep-ex].

[49] P. Stowell *et al.* (MINERvA Collaboration), Tuning the genie pion production model with minerva data, Phys. Rev. D **100**, 072005 (2019).